SIAM J. Imaging Sciences
Vol. 18, No. 2, pp. 881–905

© 2025 SIAM. Published by SIAM under the terms
of the Creative Commons 4.0 license

One Shot Inverse Scattering Revisited*

Roland Griesmaier† and Martin Hanke‡

Abstract. We develop and discuss a novel reconstruction algorithm for the inverse source problem and the inverse scattering problem for the Helmholtz equation with well-separated compactly supported sources or scatterers in two-dimensional free space from far field observations of a single radiated or scattered wave. We show that a rational approximation of a Laurent polynomial formed by the low order Fourier coefficients of the given far field pattern can be used to determine straight lines connecting the support of the sources or scatterers to the origin. After repeating this procedure for many different choices of the origin, we apply a filtered backprojection algorithm to recover information on the number and the location of the unknown sources or scatterers. We give numerical examples to illustrate the performance and limitations of our reconstruction algorithm.

Key words. inverse source problem, inverse scattering, Helmholtz equation, AAA algorithm, filtered backprojection

MSC codes. 35R30, 65N21

DOI. 10.1137/24M1709753

Downloaded 07/07/25 to 141.52.96.24 . Redistribution subject to CCBY license

1. Introduction.

We continue previous investigations [14] of rational approximation techniques for solving inverse source and inverse scattering problems for the two-dimensional time-harmonic acoustic wave equation at fixed frequency. Our goal is to recover information about the number and the positions of a few well-separated compactly supported sources or scatterers from the far field pattern of a single radiated or scattered wave. In [14] asymptotic expansions of Bessel functions for large order have been used to show that the Fourier coefficients of the far field pattern associated to high spatial frequencies can be linked to a rational function with poles that cluster near the sources or scatterers. This method, however, is very sensitive to noise, because the absolute values of the Fourier coefficients with large indices decay superlinearly, and thus most of them are below any reasonable noise level. In the present work we turn the focus from high order Fourier modes of the far field pattern to its low order modes, because these are less susceptible to data errors. Applying asymptotic expansions of Bessel functions for large argument, we link these Fourier coefficients to a rational function with poles that determine straight lines connecting the unknown sources or scatterers to the origin of the chosen coordinate system. To determine these poles numerically we solve the

*Received by the editors November 12, 2024; accepted for publication (in revised form) February 5, 2025; published electronically April 9, 2025.
https://doi.org/10.1137/24M1709753
Funding: The first author's work was partially supported by the Deutsche Forschungsgemeinschaft (DFG, German Research Foundation) – Project-ID 258734477 – SFB 1173.

†Institut für Angewandte und Numerische Mathematik, Karlsruher Institut für Technologie, 76131 Karlsruhe, Germany (roland.griesmaier@kit.edu).
‡Institut für Mathematik, Johannes Gutenberg-Universität Mainz, 55099 Mainz, Germany (hanke@math.uni-mainz.de).

© 2025 SIAM. Published by SIAM under the terms of the Creative Commons 4.0 license

rational approximation problem with the AAA algorithm of Nakatsukasa, Sète, and Trefethen [24], using a customized variant of this method that fits to our particular needs.

The given far field depends on the particular choice of the origin. However, since the background medium is assumed to be homogeneous, we can easily retrieve numerically the far field pattern with respect to any other position of the origin—henceforth called a virtual origin—by multiplication with a suitable modulating factor. Repeating the procedure outlined above for many different virtual origins yields a large number of straight lines intersecting the supports of the sources or scatterers. Parametrizing these lines by means of their normal vector and their signed distance to a (now fixed) origin, and rebinning these data on an equidistant grid on the unit cylinder, renders the possibility to apply a filtered backprojection for the Radon transform to recover information on the number and the approximate positions of the sources or scatterers.

This method works particularly well, when the far fields of the individual sources or scatterers can be approximated by far fields radiated by a rather small number of well-separated point-sources. But useful information can often also be inferred for other sources or scatterers, because the insight obtained from these reconstructions can be exploited in a subsequent step as a priori information for determining the shapes of their supporting domains. For this, one can use, e.g., iterative reconstruction schemes [17, 19] or far field splitting schemes [11, 12, 13] in combination with reconstruction algorithms for single objects like, e.g., the convex scattering support [20, 21, 29], the range test [27], or the enclosure method [15, 16].

Alternative methods for locating well-separated point-like sources or scatterers by means of sparse optimization have been addressed, e.g., by Fannjiang, Strohmer, and Yan [7] and by Pieper et al. [26]. An algorithm to estimate the number, positions, and intensities of point-sources algebraically from Cauchy data of the radiated wave has been proposed by El Badia and Nara [6]. In another scheme developed in [10] together with Raasch we have used a windowed Fourier transform of the far field pattern followed by a filtered backprojection to recover information on the supports of well-separated sources or scatterers from a single far field pattern. However, in particular at low frequencies this method gives rather blurry reconstructions. A combination of a range test algorithm and an iterative scheme based on the reciprocity gap principle for the inverse source problem has been discussed by Alves, Kress, and Serranho [1]. Finally, the no response test by Luke and Potthast [22] is a sampling method to locate scatterers from the far field pattern for a single incident wave.

The outline of this article is as follows. In section 2 we provide the problem setting for the direct and inverse source problem for the Helmholtz equation. After deriving a connection between the low order Fourier modes of the radiated far field pattern and sparse exponential sums in section 3, we use it to recover information on the location of the present sources by rational approximation. To this end we derive a special variant of the AAA algorithm in section 4, and we apply it to determine lines connecting the supports of the sources to the current origin of the coordinate system. Section 5 focuses on how this computation can be extended by considering a large number of virtual origins and on how the resulting data set can be inverted by filtered backprojection. Here we also provide a series of numerical examples. Finally, in the appendix we establish a quantitative error estimate for the approximation of the Bessel functions for large argument that we use in the derivation of the reconstruction algorithm.

Downloaded 07/07/25 to 141.52.96.24 . Redistribution subject to CCBY license

© 2025 SIAM. Published by SIAM under the terms of the Creative Commons 4.0 license

2. Problem setting. Consider the source problem

$$\Delta u + k^2 u = -f \qquad \text{in } \mathbb{R}^2 \tag{2.1}$$

for the Helmholtz equation, where f is a distribution with compact support in $\mathbb{R}^2$ and $k > 0$ denotes the wave number. The unique radiating solution u of (2.1), i.e., the distributional solution that satisfies the Sommerfeld radiation condition

$$\frac{\partial u}{\partial r} - \mathrm{i}ku = o(r^{-1/2}) \qquad \text{as } r = |x| \to \infty\,,$$

admits an asymptotic expansion

$$u(r\widehat{x}) = \frac{\mathrm{e}^{\mathrm{i}kr}}{\sqrt{kr}} \frac{\mathrm{e}^{\mathrm{i}\pi/4}}{\sqrt{8\pi}} u^\infty(\widehat{x}) + O(r^{-3/2})\,, \qquad \widehat{x} \in S^1\,, \quad \text{as } r \to \infty\,, \tag{2.2}$$

near infinity (cf., e.g., Colton and Kress [3, p. 90]). The associated function $u^\infty : S^1 \to \mathbb{C}$ is known as the far field pattern of u, or, for short, as the far field radiated by the given source f.

Here we are interested in the inverse source problem, that is, in retrieving information about the source f from knowledge of its radiated far field. Without further assumptions the source f itself cannot be retrieved from the far field pattern, as is worked out, e.g., in Bleistein and Cohen [2]. However, assuming that the individual source components are sufficiently well-separated—the diameter of each component being strictly smaller than the distance to the other components—and that each of them radiates a nontrivial far field, it has been shown by Sylvester [29] that the number and the location of these components are uniquely determined. In particular, superpositions of finitely many separated point-sources can be uniquely reconstructed.

The radiating solution u of (2.1) can be written as a volume potential

$$u(x) = \int_{\mathbb{R}^2} \Phi(x-y) f(y)\, \mathrm{d}y\,, \qquad x \in \mathbb{R}^2\,, \tag{2.3}$$

where $\Phi(x) = \frac{\mathrm{i}}{4} H_0^{(1)}(k|x|)$, $x \in \mathbb{R}^2 \setminus \{0\}$, is the radiating fundamental solution of the Helmholtz equation in $\mathbb{R}^2$, with $H_0^{(1)}$ denoting the Hankel function of the first kind of order zero. Substituting the asymptotic expansion of Hankel functions for large argument [3, p. 89], we conclude from (2.2) and (2.3) that the far field of u can be written as

$$u^\infty(\widehat{x}) = \int_{\mathbb{R}^2} \mathrm{e}^{-\mathrm{i}k\widehat{x}\cdot y} f(y)\, \mathrm{d}y\,, \qquad \widehat{x} \in S^1\,.$$

For fixed $y \in \mathbb{R}^2$ we now insert the Jacobi–Anger expansion [3, p. 91]

$$\mathrm{e}^{-\mathrm{i}k\widehat{x}_t\cdot y} = \sum_{n\in\mathbb{Z}} (-\mathrm{i})^n \mathrm{e}^{-\mathrm{i}n\arg y} J_n(k|y|)\, \mathrm{e}^{\mathrm{i}nt}\,,$$

where $\arg y$ is the polar angle of y for $y \neq 0$, and $\arg 0 = 0$, and where $\widehat{x}_t = (\cos t, \sin t)$ with $0 \le t < 2\pi$. From this we obtain the Fourier series of the far field pattern

$$u^\infty(\widehat{x}_t) = \sum_{n\in\mathbb{Z}} a_n \mathrm{e}^{\mathrm{i}nt}$$

Downloaded 07/07/25 to 141.52.96.24 . Redistribution subject to CCBY license

© 2025 SIAM. Published by SIAM under the terms of the Creative Commons 4.0 license

with

$$a_n = (-\mathrm{i})^n \int_{\mathbb{R}^2} \mathrm{e}^{-\mathrm{i}n\arg y} J_n(k|y|) f(y)\,\mathrm{d}y\,, \qquad n \in \mathbb{Z}\,. \tag{2.4}$$

Remark 2.1. Let us assume that the source f is supported in a disk of radius R around the origin. In many practically relevant situations (see [14] for point-sources, single-, and double-layer sources, and [11, 13] for square integrable sources) it has been shown that, after restricting the strength of the source and the sensitivity of the sensors that are used to measure the far fields, the observable part of the far field radiated by f belongs to a finite dimensional subspace

$$V_{\Omega_*} := \left\{ v \in L^2(S^1) \,\middle|\, v(\widehat{x}_t) = \sum_{|n|\le\Omega_*} a_n \mathrm{e}^{\mathrm{i}nt} \right\}$$

of Ω_*-bandlimited functions, where Ω_* can be chosen between kR and $3kR/2$ for a wide range of strength and sensitivity thresholds for the sources and receivers. Following [13], we refer to V_{Ω_*} as the subspace of nonevanescent far fields radiated from sources within a disk of radius R around the origin, and to the orthogonal projection $P_{\Omega_*} u^\infty$ of a far field u^∞ onto this subspace as the nonevanescent part of this far field. As suggested in [11, 12] we estimate Ω_* numerically from

$$\Omega_* \approx \Omega_\eta := \min\left\{ \Omega \,\middle|\, \|P_\Omega u^\infty\|_{L^2(S^1)} \ge (1-\eta)\|u^\infty\|_{L^2(S^1)} \right\} \tag{2.5}$$

for some sufficiently small threshold parameter $\eta > 0$, which should take the noise level into account, and then approximate

$$kR \approx \frac{2}{\mathrm{e}}\,\Omega_\eta =: kR_\eta \tag{2.6}$$

from the given data.

Example 2.2. Figure 2.1 shows the absolute values $|a_n|$ versus $n \in \mathbb{Z}$ of the Fourier coefficients of the far field to be used in Example 4.2 below, with two sources at about $(10, 10)$

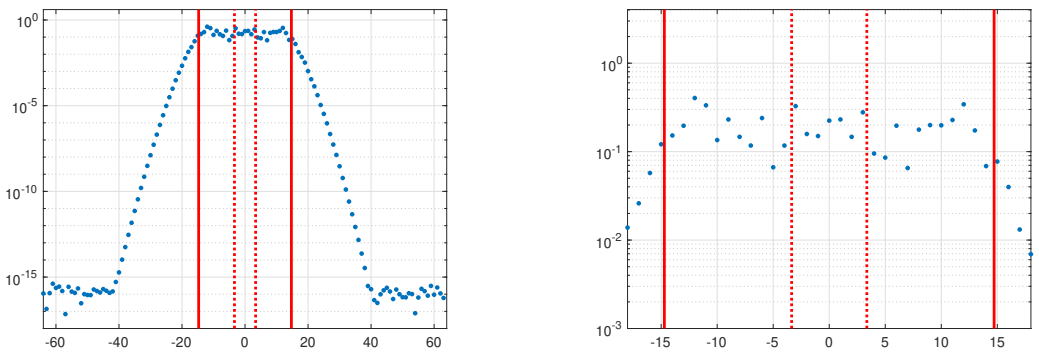

Figure 2.1. *Fourier coefficients of a particular far field (absolute values); the right hand side plot zooms in on the oscillating regime.*

Downloaded 07/07/25 to 141.52.96.24 . Redistribution subject to CCBY license

© 2025 SIAM. Published by SIAM under the terms of the Creative Commons 4.0 license

and $(6,-10)$ and wave number $k=1$. The plot exhibits the typical features of these data, as it roughly splits into three parts: The first one—bounded by the two solid vertical lines—concerns the low-frequency spectrum. This part corresponds to the frequencies associated with indices n with $|n| \lesssim kR_\eta$. Choosing $\eta = 10^{-6}$ in (2.5) gives $\Omega_* \approx \Omega_\eta = 20$. According to (2.6) we therefore obtain the estimate $kR_\eta \approx 14.72$ from this plot, while the true value is $kR \approx 14.53$. Within this range, the Fourier coefficients are oscillating, in agreement with the corresponding behavior of the Bessel functions $J_n(k|\cdot|)$ that occur in (2.4).

The second feature is the superlinear decay of the Fourier coefficients corresponding to indices n with $|n| \gtrsim kR_\eta$; we refer to this regime as the tail of this plot. And finally, when this superlinear decay has reached the order of the data noise (here, machine precision), all one can see is noise in the respective coefficients.

In [14] the evanescent part of the far field, i.e., the tail of the plot in Figure 2.1, has been used to deduce some information about the support of the source f by means of rational approximation techniques. The corresponding algorithm suffers from the fact that the information content of this tail is low for realistic noise levels, i.e., for much larger noise levels than in the plot. It is the purpose of the present paper to explore whether and how the nonevanescent component of the far field can be used instead. In fact, the algorithm which we propose below only employs the Fourier coefficients, which are enclosed by the two dotted vertical lines in Figure 2.1.

3. The idea. Consider for the moment the situation that the source f is close to a single point-source at position $y = y_0$, i.e.,

$$f \approx \gamma \delta_{y_0} \qquad \text{for some } \gamma \in \mathbb{C}\,, \tag{3.1}$$

in the sense that the far field radiated by the source f is close to the far field radiated by $\gamma\delta_{y_0}$, with δ_{y_0} denoting the delta distribution supported in y_0. Using polar coordinates

$$y_0 = r\widehat{x}_\theta = r(\cos\theta, \sin\theta)$$

with $r > 0$ and $0 \le \theta < 2\pi$ again, this means that

$$a_n \approx \gamma(-\mathrm{i})^n \mathrm{e}^{-\mathrm{i}n\theta} J_n(kr)\,, \qquad n \in \mathbb{Z}\,, \tag{3.2}$$

according to (2.4).

As we work out in the appendix, the values of the Bessel functions in (3.2) can be approximated by

$$J_n(kr) \approx \sqrt{\frac{2}{\pi kr}} \left(\cos\left(kr - \frac{\pi}{2}n - \frac{\pi}{4}\right) - \sin\left(kr - \frac{\pi}{2}n - \frac{\pi}{4}\right) \frac{4n^2-1}{8kr} \right), \tag{3.3}$$

provided that

$$|n| \le N \lesssim \sqrt{kr}\,. \tag{3.4}$$

The right hand side of (3.3) corresponds to the approximation $J_n^{(1,1)}(kr)$ considered in (A.3) in the appendix.

Downloaded 07/07/25 to 141.52.96.24 . Redistribution subject to CCBY license

© 2025 SIAM. Published by SIAM under the terms of the Creative Commons 4.0 license

Inserting (3.3) into (3.2) and rewriting sine and cosine via complex exponentials we eventually arrive at

$$a_n \approx \gamma\beta_n(\mathrm{e}^{-\mathrm{i}\theta})^n + \gamma\overline{\beta_n}(-\mathrm{e}^{-\mathrm{i}\theta})^n =: b_n\,, \qquad |n| \le N\,, \tag{3.5}$$

where

$$\beta_n = \omega_0 + \omega_1 n^2 \tag{3.6}$$

is a quadratic polynomial expression in n with coefficients

$$\omega_0 = \frac{\mathrm{e}^{\mathrm{i}\pi/4}}{\sqrt{2\pi kr}}\,\mathrm{e}^{-\mathrm{i}kr}\left(1+\frac{\mathrm{i}}{8kr}\right) \qquad \text{and} \qquad \omega_1 = \frac{\mathrm{e}^{-\mathrm{i}\pi/4}}{\sqrt{2\pi kr}}\,\mathrm{e}^{-\mathrm{i}kr}\,\frac{1}{2kr}\,. \tag{3.7}$$

Given that we are interested in the inverse source problem, we can, therefore, in principle, fix some $N \lesssim \sqrt{kr}$, use the given Fourier coefficients with indices $|n| \le N$ as data, and solve (3.5) for the unknown polar angle θ and for the coefficients $\gamma\omega_0$ and $\gamma\omega_1$; according to (3.7) one can then retrieve r from ω_0/ω_1. This is an exponential approximation problem, which is very ill-conditioned; in particular, the approximation of r will suffer severely under small uncertainties in the reconstructed value of θ.

Therefore, we restrict our efforts merely to the approximation of the exponential terms $\pm\mathrm{e}^{\mathrm{i}\theta}$ in (3.5), i.e., the polar angle of the source, and ignore the associated prefactors; note, however, that then we cannot decipher whether the polar angle of the source equals θ or $\theta\pm\pi$. To determine these two angles we apply the z-transform and define the Laurent polynomial

$$\varphi_N(z) = \sum_{n=0}^{2N} \overline{a_{n-N}}\, z^{-n-1}\,, \qquad z \in \mathbb{C}\,; \tag{3.8}$$

see Weiss and McDonough [31]. Using (3.5) we observe that

$$\begin{aligned} \varphi_N(z) \approx \psi_N(z) &:= \sum_{n=0}^{2N} \overline{b_{n-N}}\, z^{-n-1} \\ &= \overline{\gamma} \sum_{n=0}^{2N} \left(\frac{\overline{\beta_{n-N}}(\mathrm{e}^{-\mathrm{i}\theta})^N}{z}(z\mathrm{e}^{-\mathrm{i}\theta})^{-n} + \frac{\beta_{n-N}(-\mathrm{e}^{-\mathrm{i}\theta})^N}{z}(-z\mathrm{e}^{-\mathrm{i}\theta})^{-n} \right) \qquad \text{(3.9a)} \\ &\approx \overline{\gamma} \sum_{n=0}^{\infty} \left(\frac{\overline{\beta_{n-N}}(\mathrm{e}^{-\mathrm{i}\theta})^N}{z}(z\mathrm{e}^{-\mathrm{i}\theta})^{-n} + \frac{\beta_{n-N}(-\mathrm{e}^{-\mathrm{i}\theta})^N}{z}(-z\mathrm{e}^{-\mathrm{i}\theta})^{-n} \right) \qquad \text{(3.9b)} \\ &=: \psi(z) \end{aligned}$$

for $|z| > 1$. Inserting (3.6) and evaluating the series we find that

$$\begin{aligned} \psi(z) = {} & \alpha_+ \frac{1}{z-\mathrm{e}^{\mathrm{i}\theta}} + \eta_+ \frac{\mathrm{e}^{\mathrm{i}\theta}}{(z-\mathrm{e}^{\mathrm{i}\theta})^2} + \xi_+ \frac{\mathrm{e}^{\mathrm{i}\theta}(\mathrm{e}^{\mathrm{i}\theta}+z)}{(z-\mathrm{e}^{\mathrm{i}\theta})^3} \\ & + \alpha_- \frac{1}{z+\mathrm{e}^{\mathrm{i}\theta}} + \eta_- \frac{\mathrm{e}^{\mathrm{i}\theta}}{(z+\mathrm{e}^{\mathrm{i}\theta})^2} + \xi_- \frac{\mathrm{e}^{\mathrm{i}\theta}(\mathrm{e}^{\mathrm{i}\theta}-z)}{(z+\mathrm{e}^{\mathrm{i}\theta})^3} \end{aligned} \tag{3.10}$$

Downloaded 07/07/25 to 141.52.96.24 . Redistribution subject to CCBY license

© 2025 SIAM. Published by SIAM under the terms of the Creative Commons 4.0 license

with

$$\alpha_+ = \overline{\gamma}(\overline{\omega_0} + N^2\overline{\omega_1})\mathrm{e}^{-\mathrm{i}N\theta}, \qquad \alpha_- = \overline{\gamma}(\omega_0 + N^2\omega_1)(-1)^N\mathrm{e}^{-\mathrm{i}N\theta},$$
$$\eta_+ = -2\overline{\gamma}N\overline{\omega_1}\mathrm{e}^{-\mathrm{i}N\theta}, \qquad \eta_- = 2\overline{\gamma}N\omega_1(-1)^N\mathrm{e}^{-\mathrm{i}N\theta},$$
$$\xi_+ = \overline{\gamma\omega_1}\mathrm{e}^{-\mathrm{i}N\theta}, \qquad \xi_- = \overline{\gamma}\omega_1(-1)^N\mathrm{e}^{-\mathrm{i}N\theta}.$$

The important observation to make is that ψ is a rational function with two poles on the unit circle, which are symmetric with respect to the origin and whose polar angles coincide up to $\pm\pi$ with that of the source point y_0 in (3.1).

Let us be more specific about the conditions under which the rational approximation $\varphi_N \approx \psi$ in (3.9) is valid. The error in (3.9a) is due to the chosen model (3.1) in combination with the approximation (3.3) of the Bessel functions in (3.5), (3.6). Suppose that we have access to (possibly noisy) Fourier coefficients a_n of the far field radiated by f, such that

$$\frac{\pi kr}{2}\sum_{n=-N}^{N}|a_n - b_n|^2 = \delta^2. \tag{3.11}$$

The normalizing factor in front of the sum is meant to cancel the prefactor of the asymptotic representation (3.3) of the Bessel functions; therefore, δ may be interpreted as an estimate of a certain relative error in the Fourier coefficients. Then the total squared pointwise error in (3.9a) can be bounded for $|z| = \rho$ as follows:

$$\begin{aligned}|\varphi_N(z) - \psi_N(z)|^2 &\le \sum_{n=0}^{2N}|a_{n-N} - b_{n-N}|^2\sum_{n=0}^{2N}(\rho^{-n-1})^2\\ &= \frac{2}{\pi kr}\frac{\delta^2}{\rho^2}\frac{1-\rho^{-4N-2}}{1-\rho^{-2}} =: \frac{2C_\rho}{\pi kr}\frac{\delta^2}{\rho^2}.\end{aligned} \tag{3.12}$$

The estimation of the truncation error in (3.9b) is more involved: Since

$$|b_n| \le 2|\gamma||\beta_n| \le 2|\gamma|(|\omega_0| + |\omega_1|n^2)$$

by virtue of (3.5) and (3.6), the truncation error satisfies

$$\begin{aligned}|\psi(z) - \psi_N(z)| &\le \sum_{n=N+1}^{\infty}|b_n|\rho^{-N-n-1}\\ &\le 2|\gamma|\rho^{-N-1}\left(|\omega_0|\sum_{n=N+1}^{\infty}\rho^{-n} + |\omega_1|\sum_{n=N+1}^{\infty}n^2\rho^{-n}\right)\end{aligned}$$

for $|z| = \rho > 1$. Taking (3.7) into account, and evaluating the two series, this eventually leads to a bound of the form

$$|\psi(z) - \psi_N(z)| \le \frac{C_f}{\sqrt{2\pi kr}}\left(1 + \frac{N^2}{2kr}\right)\rho^{-2N-2}, \tag{3.13}$$

Downloaded 07/07/25 to 141.52.96.24 . Redistribution subject to CCBY license

© 2025 SIAM. Published by SIAM under the terms of the Creative Commons 4.0 license

where the constant C_f is a multiple of the strength $|\gamma|$ of the point-source, and hence, of $\|(a_n)_n\|_{\ell^2}$. The latter follows immediately from (3.2) and the fact that $\sum_{n\in\mathbb{Z}} J_n^2(kr) = 1$; see [5, 10.23.3]. Ideally, we want the truncation error to be smaller than the (inevitable) data and modeling error (3.12). According to (3.12) and (3.13) this is the case when

$$\rho \geq \left(\frac{1}{C_\rho^{1/2}}\frac{1}{2}\left(1+\frac{N^2}{2kr}\right)\right)^{\frac{1}{2N+1}} \left(\frac{C_f}{\delta}\right)^{\frac{1}{2N+1}}. \tag{3.14}$$

Remark 3.1. The number $2N+1$ of Fourier coefficients that we use in the definition of φ_N in (3.8) is typically small and restricted by the validity of the approximation (3.3), i.e., by the condition (3.4). According to Lemma A.1, and based on numerical tests similar to Figure A.1, somewhat larger values of N can be used when replacing $J_n^{(1,1)}(kr)$ on the right hand side of (3.3) by some $J_n^{(p,q)}(kr)$, $q \in \{p-1, p\}$, as in (A.3) with $p \gg 1$. In this case the approximation (3.9) remains valid with a rational function ψ similar to (3.10), which still has two poles on the unit circle that are symmetric with respect to the origin and whose polar angles coincide up to $\pm\pi$ with that of the source point y_0 in (3.1). The only difference is that these poles then come with multiplicities up to order $2(p+q)-1$ instead of three. However, this does not affect the reconstruction of the polar angle of the source point, which is obtained by the algorithm that we develop next in section 4 below. Therefore, using a few more Fourier coefficients than determined by (3.4) is also justified. We will make use of this observation in Examples 5.4 and 5.5 in section 5.

Of course, the presentation above is rather simplified in that we have made the assumption that a single point-source can be used as an effective model for the true source f. Since our real interest is in the case of several separated sources, we now turn to the case where a combination of a finite number of point-sources is needed for a good approximation of f, i.e., we assume that

$$f \approx \sum_{j=1}^{J} \gamma_j \delta_{y_j}, \qquad y_j = r_j\, \widehat{x}_{\theta_j}, \tag{3.15}$$

for some small $J \in \mathbb{N}$, where $r_j > 0$, $0 \leq \theta_j < 2\pi$, and $\gamma_j \in \mathbb{C}$. In this case we proceed similarly and truncate the Laurent polynomial (3.8) after

$$N \lesssim \min_j \sqrt{kr_j} \tag{3.16}$$

terms. Then, since the solution of the source problem, the Fourier coefficients of its far field, and the definition of the Laurent polynomial (3.8) all depend linearly on the source, we obtain by superposition that the resulting Laurent polynomial φ_N is close to a rational function ψ with poles in $\pm e^{i\theta_j}$, meaning that

$$|\varphi_N(z) - \psi(z)| \leq \frac{4}{N}\left(\frac{C_\rho}{2\pi}\right)^{1/2}\frac{\delta}{\rho} \qquad \text{for } |z| = \rho, \tag{3.17}$$

provided that $\rho > 1$ satisfies the inequality (3.14) and N satisfies (3.16).

Downloaded 07/07/25 to 141.52.96.24 . Redistribution subject to CCBY license

© 2025 SIAM. Published by SIAM under the terms of the Creative Commons 4.0 license

Downloaded 07/07/25 to 141.52.96.24 . Redistribution subject to CCBY license

We summarize our findings of this section. Assuming that the source f is well approximated by a combination of finitely many point-sources, then the Laurent polynomial (3.8) agrees up to the relative modeling and data error (3.17) with a rational function whose poles provide the polar angles of the individual sources. This is true for all z in the exterior of a disk of radius $\rho > 1$ around the origin in the complex plane, as long as ρ satisfies the inequality (3.14), which depends on the strength of the sources and the amount of errors in the data, and in particular, on the number of terms of the Laurent polynomial.

The above analysis suggests to recover the polar angles θ_j of the source points y_j by (i) approximating φ_N on some circle $|z| = \rho > 1$ numerically by a rational function with poles on or close to the unit circle and (ii) by using these poles as estimates of $\pm e^{i\theta_j}$. Take note that φ_N in itself is a rational function with a single pole (of order $2N+1$) at the origin; the crucial point is therefore to approximate φ_N by a rational function of smaller (denominator) degree with poles close to the unit circle.

Remark 3.2. The definition (3.8) of the Laurent polynomial φ_N is not symmetric with respect to the order of the Fourier coefficients $a_{-N}, \dots, a_N$. When evaluating $\varphi_N(z)$ at $z \in \mathbb{C}$ with $|z| = \rho > 1$ the information content of the Fourier coefficients with positive indices is much more damped compared to that within the coefficients with negative indices. This is somewhat unsatisfactory. Reversing the order of the Fourier coefficients, we can alternatively consider

$$\widetilde{\varphi}_N(z) = \sum_{n=0}^{2N} a_{N-n} z^{-n-1}, \qquad z \in \mathbb{C}. \tag{3.18}$$

Applying the same arguments as in (3.9) we obtain that, for $|z| = \rho > 1$, this Laurent polynomial satisfies $\widetilde{\varphi}_N(z) \approx \widetilde{\psi}(z)$, where the rational function

$$\begin{aligned}\widetilde{\psi}(z) = \sum_{j=1}^{J} \Bigg(& \widetilde{\alpha}_j \frac{1}{z - e^{i\theta_j}} + \widetilde{\eta}_j \frac{e^{i\theta_j}}{(z - e^{i\theta_j})^2} + \widetilde{\xi}_j \frac{e^{i\theta_j}(e^{i\theta_j} + z)}{(z - e^{i\theta_j})^3} \\ & + \widetilde{\alpha}_{-j} \frac{1}{z + e^{i\theta_j}} + \widetilde{\eta}_{-j} \frac{e^{i\theta_j}}{(z + e^{i\theta_j})^2} + \widetilde{\xi}_{-j} \frac{e^{i\theta_j}(e^{i\theta_j} - z)}{(z + e^{i\theta_j})^3} \Bigg)\end{aligned}$$

has coefficients

$$\begin{aligned}\widetilde{\alpha}_j &= \gamma_j(\omega_{j,0} + N^2\omega_{j,1})e^{-iN\theta_j}, & \widetilde{\alpha}_{-j} &= \gamma_j(\overline{\omega_{j,0}} + N^2\overline{\omega_{j,1}})(-1)^N e^{-iN\theta_j}, \\ \widetilde{\eta}_j &= -\gamma_j 2N\omega_{j,1} e^{-iN\theta_j}, & \widetilde{\eta}_{-j} &= \gamma_j 2N\overline{\omega_{j,1}}(-1)^N e^{-iN\theta_j}, \\ \widetilde{\xi}_j &= \gamma_j \omega_{j,1} e^{-iN\theta_j}, & \widetilde{\xi}_{-j} &= \gamma_j \overline{\omega_{j,1}}(-1)^N e^{-iN\theta_j},\end{aligned}$$

and the same poles as ψ. In our numerical examples in section 5 we will not only use φ_N but also $\widetilde{\varphi}_N$ as well as $(\varphi_N + \widetilde{\varphi}_N)/2$ and $(\varphi_N - \widetilde{\varphi}_N)/2$ to symmetrize the usage of the Fourier data in the reconstruction algorithm.

4. A special variant of the AAA algorithm. To determine a suitable rational approximation of the Laurent polynomial φ_N we suggest the AAA algorithm, which has been proposed

© 2025 SIAM. Published by SIAM under the terms of the Creative Commons 4.0 license

in [24] as a powerful tool for rational approximation. This algorithm determines a rational function which matches a set of given function values of φ_N to a prescribed tolerance.

In view of the discussion in the previous section these function values should correspond to arguments $z \in \mathbb{C}$ whose absolute value $|z| = \rho > 1$ satisfies (3.14). Moreover, $|z|$ should not be too large in order to extract most of the information content hidden in all relevant Fourier coefficients a_n with $|n| \le N$. Concerning the terms occurring in (3.14), take note that $1 \le C_\rho \le 2N+1$ by virtue of (3.12), and hence $1 \le C_\rho^{1/(4N+2)} \le \exp(1/(2\mathrm{e})) < 1.202$; further note that $N^2/(kr)$ is about one in view of (3.16). Finally, we choose $4\,\|(a_n)_n\|_{\ell^2}$ for the value of the constant C_f on the grounds of the derivation of (3.13). Accordingly we replace the right hand side of (3.14) by

$$\rho_* := (4\,\|(a_n)_n\|_{\ell^2}/\delta)^{\frac{1}{2N+1}} \tag{4.1}$$

in our numerical code. To estimate the value of δ in (3.11), we use a guess for the relative data and modeling error $\Delta e := (\sum_{|n|\le N} |a_n - b_n|^2 / \sum_{|n|\le N} |a_n|^2)^{1/2}$ and then approximate

$$\delta \approx \Delta e \left(\frac{\pi N^2}{2} \sum_{n=-N}^{N} |a_n|^2 \right)^{1/2} . \tag{4.2}$$

Therewith, we can evaluate (4.1) and choose the input arguments for the AAA algorithm from the circle $|z| = \rho_*$. More precisely, we determine the function values $y_\nu = \varphi_N(z_\nu)$ for an equidistant angular grid

$$z_{\pm\nu} = \pm\rho_* \, \mathrm{e}^{\mathrm{i}\nu\pi/M} , \qquad \nu = 1, \dots, M , \tag{4.3}$$

with $2M$ points on this circle. In view of (3.17) we then aim for a fit of order

$$\tau := \frac{2}{N} \left(\frac{C_{\rho_*}}{2\pi} \right)^{1/2} \frac{\delta}{\rho_*} \tag{4.4}$$

of these data. We note that this threshold is smaller by a factor of $1/2$ than the right hand side of (3.17), but this slight overfitting has yielded better numerical results. The reason is that when the tolerance is too loose then the AAA algorithm will often terminate with small degree rational functions and therefore does not provide enough pole information. Alternatively, one may take this factor $1/2$ as a compensation for the overestimation of the true error in (3.9) by using upper bounds.

Remark 4.1. We mention in passing that the underlying approach is similar to a method for parameter estimation for sparse exponential sums suggested by Derevianko, Plonka, and Petz [4]. However, the number of terms of the Laurent polynomial φ_N used in [4] is larger by orders of magnitude, so that a fine angular spacing of the grid points z_ν of (4.3) could be achieved in [4] by choosing all $(2N+1)$th complex roots of ρ^{2N+1}. For this particular grid the associated function values coincide with those of another rational function with the same poles, so that the approximation (3.9b) is no longer necessary. This is the major difference in our setting here, because it enables the choice $\rho = 1$ utilized in [4]. In our application the

Downloaded 07/07/25 to 141.52.96.24 . Redistribution subject to CCBY license

© 2025 SIAM. Published by SIAM under the terms of the Creative Commons 4.0 license

corresponding number of input data pairs for the AAA algorithm would be much smaller, namely, at most ten to twenty. We did some numerical experiments with the method in [4] and found that the corresponding rational approximations are not sufficient for our purposes.

In the original paper [24] the rational function determined by the AAA algorithm is represented in barycentric form, i.e.,

$$\mathcal{R}(z) = \sum_{\nu\in\mathcal{N}} \frac{w_\nu y_\nu}{z - z_\nu} \Bigg/ \sum_{\nu\in\mathcal{N}} \frac{w_\nu}{z - z_\nu}\,, \tag{4.5}$$

with appropriate (complex) parameters $w_\nu \neq 0$, $\nu \in \mathcal{N}$. As observed earlier (cf., e.g., Schneider and Werner [28]), a rational function of the form (4.5) interpolates by construction the data points $(z_\nu|y_\nu)$ with $\nu \in \mathcal{N} \subset \{\pm 1, \ldots, \pm M\}$. In the AAA scheme the parameters w_ν are chosen in such a way that the fit for the remaining data points is optimal in an appropriate sense; compare (4.7) below. However, since φ_N is no even function in general, the poles of this rational approximation will not be symmetric with respect to the origin. Another issue with (4.5) is that although ψ of (3.10) vanishes at infinity, the generic AAA approximation will not.

We therefore replace (4.5) by the Ansatz

$$\mathcal{R}(z) = \sum_{\nu\in\mathcal{N}_+} w_\nu \left(\frac{y_\nu}{z - z_\nu} - \frac{y_{-\nu}}{z + z_\nu}\right) \Bigg/ \left(w_\infty + \sum_{\nu\in\mathcal{N}_+} w_\nu \left(\frac{1}{z - z_\nu} - \frac{1}{z + z_\nu}\right)\right), \tag{4.6}$$

where $\mathcal{N}_+ \subset \{1, \ldots, M\}$: Similar to the original version (4.5) this function interpolates the data points $(z_\nu|y_\nu)$ with $|\nu| \in \mathcal{N}_+$; moreover, unless $w_\infty = 0$, the rational approximation (4.6) vanishes at infinity, and since its denominator is an even function, the zeros of the latter—which constitute the poles of $\mathcal{R}$—are symmetric with respect to the origin.

Let

$$\mathcal{M} = \{\pm 1, \ldots, \pm M\} \setminus \{\nu : |\nu| \in \mathcal{N}_+\}$$

be the indices of the data points which are not used for interpolation, and define $w = [w_\nu]_{\nu\in\mathcal{N}_+}$ and $y = [y_\mu]_{\mu\in\mathcal{M}}$. Then, following the derivation of the original AAA algorithm, the parameters w_ν, $\nu \in \mathcal{N}_+$, and w_∞ are chosen such that the quadratic form

$$\|w_\infty y + \Delta L\, w\|_2^2 \tag{4.7}$$

becomes minimal, subject to the constraint

$$|w_\infty|^2 + \|w\|_2^2 = 1\,,$$

where the matrix ΔL is given by

$$\Delta L = \left[\frac{y_\mu - y_\nu}{z_\mu - z_\nu} - \frac{y_\mu - y_{-\nu}}{z_\mu + z_\nu}\right]_{\mu\in\mathcal{M},\,\nu\in\mathcal{N}_+}.$$

Downloaded 07/07/25 to 141.52.96.24 . Redistribution subject to CCBY license

© 2025 SIAM. Published by SIAM under the terms of the Creative Commons 4.0 license

In other words, the vector $[w_\infty, w_\nu]^T_{\nu\in\mathcal{N}_+}$ is a singular vector associated with the smallest singular value of the matrix

$$W = [y \quad \Delta L].$$

The list of indices in $\mathcal{N}_+$, which determines the set of data points that are used for interpolation rather than approximation, is determined by a greedy iteration in the AAA scheme: Starting with an empty set $\mathcal{N}_+ = \emptyset$, the absolute value of an index ν, for which the current residual $|y_\nu - \mathcal{R}(z_\nu)|$ is largest, is appended after each iteration to the list of indices in $\mathcal{N}_+$, until, eventually, all the residuals are below the tolerance τ of (4.4).

The poles of the final approximation $\mathcal{R}$ of (4.6) are the finite eigenvalues $\lambda \in \mathbb{C}$ of the matrix pencil

$$\begin{bmatrix} w_\infty & 1 \cdots 1 & 1 \cdots 1 \\ w & Z - \lambda I & 0 \\ -w & 0 & -Z - \lambda I \end{bmatrix},$$

where Z is the diagonal matrix with the interpolation grid points z_ν, $\nu \in \mathcal{N}_+$, on the diagonal. This can readily be checked by computing the corresponding eigenvector. Of course, there is no guarantee that these poles are located on the unit circle, and we discard poles as spurious ones, when they fail to belong to the annulus

$$0.95 < |z| < 1.05\,.$$

Example 4.2. To illustrate the method we consider an incident time-harmonic plane wave with direction of propagation $(1, 0)$ in a homogeneous medium with wave number $k = 1$, which is scattered by two objects with a diameter of about one, namely, a kite located at $(10, 10)$ and a disk at $(6, -10)$: The kite is a sound-soft scatterer,[1] whereas the disk is such that the total field satisfies a homogeneous impedance condition.[2] We simulate the far field pattern of the scattered wave with a Nyström method as described in [3, 18], using an equidistant grid on S^1 with 128 points. The scattered wave u solves the source problem (2.1) for some (distributional) source f supported on the boundaries of the two scatterers. In fact, since the scatterers are relatively small compared to the wavelength of the incident field (the diameters of the kite and the circle are 0.22 and 0.13 wavelengths, respectively), the associated far field pattern can be approximated by the far field radiated by two point-sources supported near the centers of the two scatterers as in (3.15) rather well (see, e.g., [9, Thm. 3.1]).

The absolute values of the Fourier coefficients of the far field of the corresponding scattered wave have already been displayed in Figure 2.1. Figure 4.1 shows the two scatterers and the disk with radius $r_* \approx 11.26$, which is the minimal distance of the scatterers from the origin. Accordingly, we use seven Fourier coefficients a_n (corresponding to $N = 3 = \lfloor\sqrt{11.26}\rfloor$ in accordance with (3.16)) for the Laurent polynomial φ_N; they belong to the oscillating regime

[1] See, e.g., [3, p. 2].
[2] See, e.g., [3, p. 3]. We use the value $\lambda = 0.5$ for the impedance parameter.

Downloaded 07/07/25 to 141.52.96.24 . Redistribution subject to CCBY license

© 2025 SIAM. Published by SIAM under the terms of the Creative Commons 4.0 license

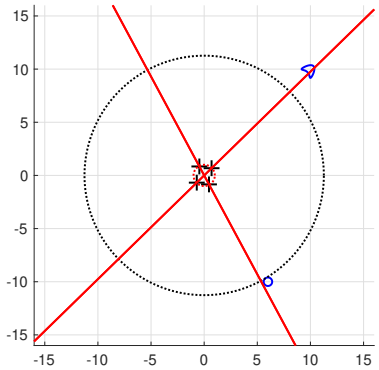

Figure 4.1. *Illustration of the basic algorithm for Example 4.2.*

of the Fourier coefficients as indicated by the dotted red bars in Figure 2.1. (Color images are available online.)

With the estimated value $\Delta e = 10^{-3}$ in (4.2) the radius (4.1) of the circle, on which φ_N is being evaluated, has been determined to be $\rho_* \approx 3.33$ by (4.1). We use $2M = 100$ data pairs on this circle as input for the modified AAA algorithm. The tolerance τ in the AAA algorithm is $7.18 \cdot 10^{-5}$ according to (4.4). The greedy AAA iteration determines a rational approximation with four poles.

Figure 4.1 shows these poles marked as black crosses, which are all close to the unit circle. According to the theory the scatterers should be located along the red lines, which depict all complex numbers which share the polar angle with one of the four poles. In this particular example these two lines indeed (almost) intersect the two scatterers.

5. Moving around. To get further information about the location of the sources we can utilize another important property of the inverse source problem that has, e.g., been advocated by Kusiak and Sylvester in [21] (see also [22, 27]), and that has already been employed in [14] as well. Assume that we shift the origin of the coordinate system to some arbitrary point $c \in \mathbb{R}^2$, or rather, keep the origin and move the source f, so that we consider the radiating solution u_c of the Helmholtz equation (2.1) with f replaced by the (virtual) source f_c given by

$$f_c(y) = f(c+y)\,, \qquad y \in \mathbb{R}^2\,.$$

A straightforward computation reveals that this solution has the far field pattern

$$u_c^\infty(\widehat{x}) = \mathrm{e}^{\mathrm{i}kc\cdot\widehat{x}} u^\infty(\widehat{x})\,, \qquad \widehat{x} \in S^1\,, \tag{5.1}$$

which is immediately available from the given data u^∞—and so are its Fourier coefficients

$$a_n^c = \sum_{m\in\mathbb{Z}} \mathrm{i}^{m-n} \mathrm{e}^{\mathrm{i}(m-n)\arg c} J_{m-n}(k|c|) a_m\,, \qquad n \in \mathbb{Z}\,.$$

Remark 5.1. Assuming that f is supported in a disk of radius $R > 0$ and that we can only observe the nonevanescent part of its radiated far field u^∞, we have argued in Remark 2.1 that

Downloaded 07/07/25 to 141.52.96.24 . Redistribution subject to CCBY license

© 2025 SIAM. Published by SIAM under the terms of the Creative Commons 4.0 license

$2\Omega_* + 1$ Fourier coefficients of the far field pattern for some $\Omega_* \gtrsim kR$ suffice to capture all the information from u^∞. In our numerical examples below we will simulate the far field patterns on a sufficiently fine grid to be able to compute these Fourier coefficients with satisfactory accuracy. According to the Shannon sampling theorem (cf., e.g., Natterer and Wübbeling [25, p. 67]), this is the case if our equidistant angular grid has at least $2\Omega_*$ grid points.

Depending on the shift parameter c in (5.1), the radius R_c of the smallest disk centered at zero that contains the support of the shifted source f_c might be significantly larger than R. As a consequence, the number $2\Omega_*^c + 1$ of Fourier coefficients with $\Omega_*^c \gtrsim kR_c$ that are required to correctly represent the radiated far field u_c^∞ might be significantly larger than the number of Fourier coefficients which are available from our simulated far field data. However, since the Fourier coefficients of the original far field are essentially zero for $|n| > \Omega_*$ we can employ the approximation

$$a_n^c \approx \sum_{m=-\Omega_*}^{\Omega_*} \mathrm{i}^{m-n} \mathrm{e}^{\mathrm{i}(m-n)\arg c} J_{m-n}(k|c|) a_m \,, \qquad n = -\Omega_*^c, \dots, \Omega_*^c \,,$$

to determine the Fourier coefficients of u_c^∞ to sufficient accuracy.

When we apply the algorithm developed in the previous sections to the far field pattern u_c^∞ we obtain lines which connect the virtual origin c with approximate locations of individual source components. Repeating this procedure for many different virtual origins $c \in \Lambda$, where $\Lambda \subseteq \mathbb{R}^2$ denotes some suitable grid of points, gives a large number of lines, each of which should intersect or be at least close to one source component.

Each line ℓ recovered by the scheme outlined above can be represented in the form

$$\ell(\omega, s) := \{ s\omega + t\omega^\perp \,|\, t \in \mathbb{R} \} \,,$$

parametrized by a normal vector $\omega \in S^1$ and the associated signed distance $s \in \mathbb{R}$ from the true origin. Next, we consider the grid

$$\Sigma := \{ (\omega_h, s_l) \,|\, h = 0, \dots, 2H-1 \,,\, l = -L, \dots, L \} \subseteq S^1 \times \mathbb{R} \tag{5.2}$$

with

$$\omega_h = (\cos(h\Delta\omega), \sin(h\Delta\omega)) \qquad \text{and} \qquad s_l = l\Delta s \,,$$

where $\Delta\omega = \pi/H$ and $\Delta s = d/(L\sqrt{2})$ for some $H, L \in \mathbb{N}$. Here $d > 0$ denotes the side length of a square region of interest, in which we want to reconstruct the support of the sources. For each line $\ell(\omega, s)$ that is recovered by the AAA algorithm we first determine the nearest normal direction ω_{h_*} in the grid Σ from (5.2), i.e.,

$$|\omega - \omega_{h_*}| = \min\{ |\omega - \omega_h| \,|\, h = 0 \dots, 2H-1 \} \,,$$

and we set $h_{**} = (h_* + N) \bmod 2N$; note that $\ell(\omega_{h_*}, s) = \ell(\omega_{h_{**}}, -s)$. Then we define a matrix $R^{\ell(\omega,s)} \in \mathbb{R}^{(2L+1)\times H}$ with entries

$$R_{l,h}^{\ell(\omega,s)} = \begin{cases} \dfrac{\varepsilon}{\sqrt{2\pi}} \mathrm{e}^{-\frac{1}{2}|s-s_l|^2\varepsilon^2} & \text{if } h = h_* \text{ and } l = -L, \dots, L \,, \\ \dfrac{\varepsilon}{\sqrt{2\pi}} \mathrm{e}^{-\frac{1}{2}|-s-s_l|^2\varepsilon^2} & \text{if } h = h_{**} \text{ and } l = -L, \dots, L \,, \\ 0 & \text{else} \,. \end{cases} \tag{5.3}$$

Downloaded 07/07/25 to 141.52.96.24 . Redistribution subject to CCBY license

© 2025 SIAM. Published by SIAM under the terms of the Creative Commons 4.0 license

A similar Gaussian spreading is often used in nonuniform fast Fourier transforms; see, e.g., Greengard and Lee [8]. The h_*th and the h_{**}th column of $R^{\ell(\omega,s)}$ are discretized one-dimensional Gaussians with standard deviation $1/\varepsilon$, and we interpret these as probability densities describing whether there is a source located along a line orthogonal to ω_{h_*} with signed distance s_l from the true origin. We further note that the h_*th and the h_{**}th column of $R^{\ell(\omega,s)}$ coincide with the h_*th and the h_{**}th column of the values of the Radon transform of $g_\varepsilon(\cdot - z)$ on Σ, respectively, where

$$g_\varepsilon(x) = \frac{\varepsilon^2}{2\pi} \mathrm{e}^{-\frac{1}{2}|x|^2\varepsilon^2}, \qquad x \in \mathbb{R}^2,$$

is a two-dimensional Gaussian with standard deviation $1/\varepsilon$ and z is any point on $\ell(\omega_{h_*}, s)$. Accordingly, when adding up these matrices $R^{\ell(\omega,s)}$ for all lines $\ell(\omega, s)$ that have been determined by the AAA algorithm for all possible virtual origins $c \in \Lambda$, the result should be close to the values on Σ of the Radon transform of some density function with peaks near the individual supports of the sources and negligible magnitude away from them. Since we have spread every single pole information via the particular ansatz (5.3) to neighboring parallel lines, we may further expect that this density function has an essential bandwidth of roughly 3ε.

We now apply the classical filtered backprojection algorithm for the two-dimensional Radon transform, as described, e.g., in [25, pp. 81–87], to reconstruct this density function in order to visualize the support of the sources. The aforementioned guess 3ε of the bandwidth of this function is used as parameter for the Ram–Lak filter in this algorithm. Accordingly, [25, p. 86] suggests the sampling conditions

$$\Delta s \le \frac{\pi}{3\varepsilon} \qquad \text{and} \qquad \Delta\omega \le \frac{\sqrt{2}}{d}\frac{\pi}{3\varepsilon} \tag{5.4}$$

for the grid Σ in (5.2) to obtain artifact free reconstructions.

Remark 5.2. We have already mentioned in Remark 3.2 that there are at least four different ways to define a Laurent polynomial from the given far field data, which can then be used as input for the AAA algorithm. To symmetrize the use of the Fourier coefficients and to stabilize the reconstruction algorithm in our numerical examples below, we run the AAA algorithm for each virtual origin $c \in \Lambda$ four times using φ_N from (3.8), $\widetilde{\varphi}_N$ from (3.18), as well as $(\varphi_N + \widetilde{\varphi}_N)/2$ and $(\varphi_N - \widetilde{\varphi}_N)/2$ as input data. Each of these four computations typically gives a slightly different set of lines indicating the directions of the scatterers, when seen from the current virtual origin. We then simply combine all the reconstructed lines obtained for the four different versions of the Laurent polynomial into one discrete sinogram by adding up all associated matrices R^ℓ from (5.3) for all virtual origins $c \in \Lambda$.

Example 5.3. We continue with Example 4.2, but this time we simulate the far field pattern of the scattered field on an equidistant grid with just 64 points on S^1, which is sufficient according to Remark 2.1 and Example 2.2. We choose 900 virtual origins that are equiangularly distributed on a grid Λ on five circles around the true origin with radii $25, 26, \ldots, 29$ as visualized by the red crosses in Figure 5.1 (left). We have already obtained the estimate $R_\eta \approx 14.72$ for the radius of the smallest disk centered at the origin that contains

Downloaded 07/07/25 to 141.52.96.24 . Redistribution subject to CCBY license

© 2025 SIAM. Published by SIAM under the terms of the Creative Commons 4.0 license

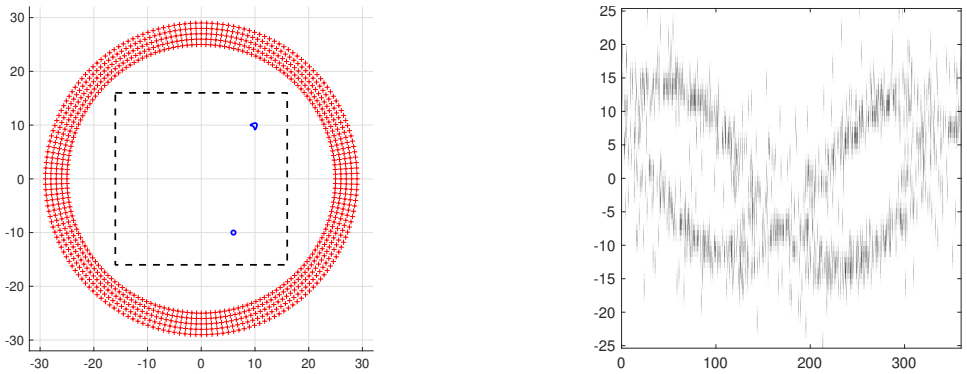

Figure 5.1. *Geometrical setup of Example 5.3 (left); sinogram from unperturbed data (right).*

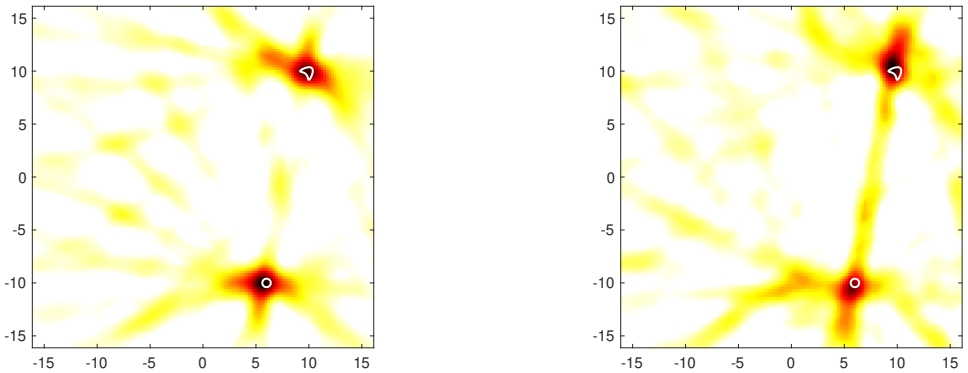

Figure 5.2. *Reconstruction from unperturbed data in Example 5.3 (left); reconstruction from noisy data with 5% uniformly distributed relative error (right).*

the scatterers in Example 2.2. Accordingly, the distance between each virtual origin $c \in \Lambda$ and the scatterers is approximately bounded from below by $|c| - R_\eta$. Therefore, we set $N = \lfloor (k(|c| - R_\eta))^{1/2} \rfloor$ and use $2N + 1$ Fourier coefficients a_n^c of the translated far field u_c^∞ for the corresponding Laurent polynomials φ_N, $\widetilde{\varphi}_N$, $(\varphi_N + \widetilde{\varphi}_N)/2$, and $(\varphi_N - \widetilde{\varphi}_N)/2$ for each virtual origin $c \in \Lambda$. We choose $\Delta e = 10^{-3}$ for the estimated relative error in (4.2), and we determine the radius ρ_* in (4.3) according to (4.1) and the tolerance τ in the AAA algorithm according to (4.4). As mentioned before, we use $2M = 100$ data pairs on the circle of radius ρ_* as input for the AAA algorithm.

We take $d = 32$ for the side length of the region of interest, which is shown as a dashed square in Figure 5.1 (left). For the other parameters in the rebinning and filtered backprojection scheme, we use $\varepsilon = 1.3$ and determine Δs and $\Delta\omega$ according to (5.4). The plot in Figure 5.1 (right) shows the resulting sinogram (i.e., the sum of all matrices $R^{\ell(\omega,s)}$ for all virtual origins and the four realizations of the corresponding Laurent polynomials). We note that this sinogram consists of 63 rows and 5057 columns in agreement with (5.4). The reconstruction of the source positions obtained by the filtered backprojection is shown in Figure 5.2 (left) together with visualizations of the true locations of the scatterers. Here and in all following examples, negative values in the reconstruction have been replaced by zero.

Downloaded 07/07/25 to 141.52.96.24 . Redistribution subject to CCBY license

© 2025 SIAM. Published by SIAM under the terms of the Creative Commons 4.0 license

We would like to elaborate briefly on this sinogram. It is well-known that the Radon transform sinogram of a point-source shows the graph of a shifted sine function with a certain amplitude; the sinogram of a Gaussian centered at the same point is a "sine ribbon," i.e., a Gaussian blur in vertical direction of the former graph; see [10]. In the particular plot in Figure 5.1 one can easily identify two sine ribbons corresponding to the two source components of our phantom. But it can also be seen that this plot contains a decent amount of aberrations and outliers, which are due to inaccurate reconstructions of pole directions due to the AAA algorithm. Aside from this there are gaps in the two sine ribbons near their crossing points: Apparently the rational approximations fail to provide accurate pole information, when the two double cones connecting a virtual origin with the individual source components are close to each other. In this case the exponential terms associated to these two source components according to (3.2) might interfere strongly.

To study the sensitivity of the reconstruction algorithm with respect to noise in the data, we repeat the computations but add 5% complex-valued uniformly distributed relative error to the original far field data. Figure 5.2 (right) shows the corresponding results. We use the same parameters as before, except for η and Δe (which then also implies new values for δ, ρ_*, and τ according to (4.2), (4.1), and (4.4)). Taking into account the magnitude of the relative data error, we choose $\eta = 2 \cdot 10^{-3}$ and $\Delta e = 0.025$. The reconstructions are only slightly worse than those obtained in the noise free case.

Example 5.4. In our second example, we add a third scatterer to the scene, which is a sound-hard[3] ellipse at $(-10, 0)$, the diameter of the ellipse being 0.38 wavelengths. We consider again a plane wave incident field with wave number $k = 1$ and direction of propagation $(1, 0)$ and simulate the far field pattern of the scattered wave in the same way as before. The main difference in Example 5.3 is that we use a different setup for the virtual origins in that we select 2500 equidistant points on a square cartesian grid Λ with side length 40 as shown in Figure 5.3 (left). Since we can now no longer bound the distance of the virtual origins from the scatterers from below, we have to relax the condition (3.16). Instead we estimate for each virtual origin $c \in \Lambda$ the radius $R_\eta^{(c)}$ of the smallest disk centered at c containing all scatterers

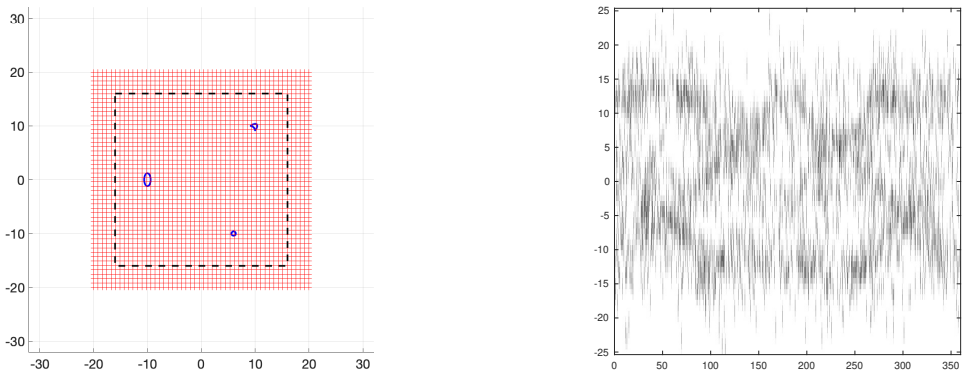

Figure 5.3. *Geometrical setup of Example 5.4 (left); sinogram from unperturbed data (right).*

[3]See, e.g., [3, p. 2].

Downloaded 07/07/25 to 141.52.96.24 . Redistribution subject to CCBY license

© 2025 SIAM. Published by SIAM under the terms of the Creative Commons 4.0 license

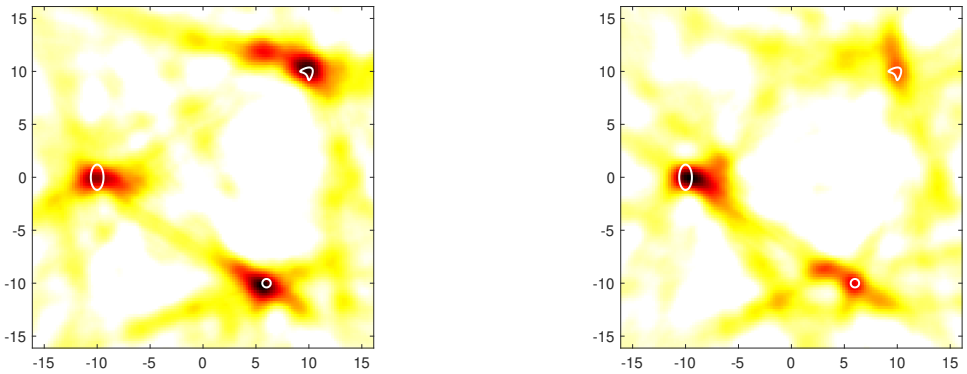

Figure 5.4. *Reconstruction from unperturbed data in Example 5.4 (left); reconstruction from noisy data with 5% uniformly distributed relative error (right).*

by means of (2.5), (2.6), let $N = \lfloor (kR_\eta^{(c)})^{1/2} \rfloor - 1$, and use $2N+1$ Fourier coefficients a_n^c of the translated far field u_c^∞ for the corresponding Laurent polynomials. To some extent this is justified by Remark 3.1, and numerical tests have confirmed that this strategy actually works much better than the circular grid of virtual origins in Example 5.3 in cases of more than two scatterers—as long as they are sufficiently well-separated. We choose $\Delta e = 10^{-3}$ for the estimated relative error in (4.2), and we determine the radius ρ_* by (4.1) and the tolerance τ by (4.4). Again, we use $2M = 100$ data pairs on the circle of radius ρ_* as input for the modified AAA algorithm.

The region of interest, which is shown as a dashed square in Figure 5.3 (left), and the other parameters in the rebinning and filtered backprojection scheme remain the same as in Example 5.3. The corresponding sinogram is shown in Figure 5.3 (right). The reconstructions of the source positions that we have obtained by the filtered backprojection are shown in Figure 5.4 (left) together with visualizations of the true locations of the small scatterers.

As in Example 5.3 we repeat the computation for noisy far field data containing 5% uniformly distributed relative additive error. Accordingly, we choose $\eta = 2 \cdot 10^{-3}$ and $\Delta e = 0.025$ as in the noise case of Example 5.3, and otherwise we use the same parameters as before. The results are shown in Figure 5.4 (right). The reconstructions of the additional circular scatterer and of the kite-shaped scatterer are less pronounced than in the noise free case, but it still seems possible to correctly guess the locations of the three scatterers.

Example 5.5. In our third example we consider three larger scattering objects: two sound-hard obstacles at $(10, 10)$ and $(8, -10)$, and a sound-soft obstacle at $(-8, 0)$ as shown in Figure 5.5 (left). We consider a plane wave incident field with wave number $k = 1$ and direction of propagation $(1, 0)$ and simulate the far field pattern of the scattered field on the same equidistant grid with 64 points on S^1 as before. Here we are no longer close to the point-scatterer regime, because the wavelength $\lambda \approx 6.28$ is comparable to the diameter of the obstacles (the diameters of the kite, the ellipse, and the nut are 1.35, 0.64, and 0.83 wavelengths, respectively). We use the same grid for the virtual origins, the same region of interest for the reconstructions, and the same parameters for the reconstruction algorithm as in Example 5.4. The corresponding sinogram is shown in Figure 5.5 (right).

Downloaded 07/07/25 to 141.52.96.24 . Redistribution subject to CCBY license

© 2025 SIAM. Published by SIAM under the terms of the Creative Commons 4.0 license

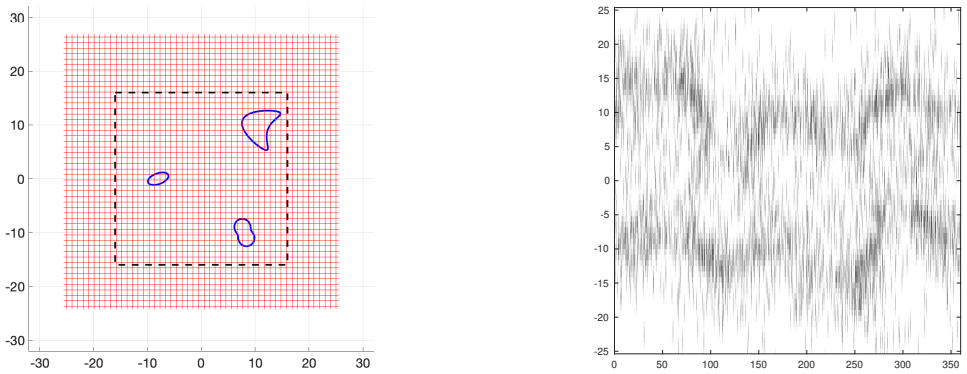

Figure 5.5. *Geometrical setup of Example 5.5 (left); sinogram from unperturbed data (right).*

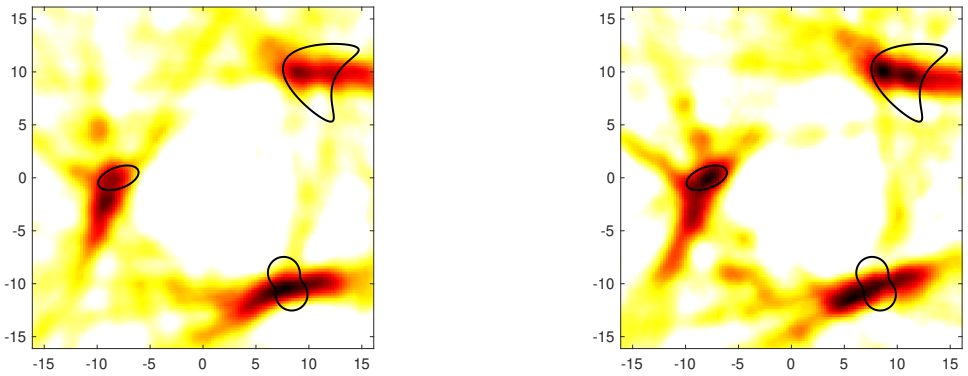

Figure 5.6. *Reconstruction from unperturbed data in Example 5.5 (left); reconstruction from noisy data with 5% uniformly distributed relative error (right).*

The reconstructions of the source locations obtained from unperturbed data and from noisy far field data containing 5% uniformly distributed relative additive error are shown together with visualizations of the true locations of the scatterers in Figure 5.6. Although the shape of the scatterers cannot be inferred from these reconstructions, even with 5% noise on the data the correct number and the approximate locations of the scatterers can easily be depicted.

Example 5.6. In our numerical results so far we have considered $k = 1$ for the wave number, and the scatterers have been chosen such that their diameters were either less than or comparable to the wavelength. This regime is usually called the resonance region, and it is the regime we are mainly interested in. Nevertheless, we repeat in our final example Examples 5.3–5.5, but this time we apply the reconstruction method at wave number $k = 10$ instead of $k = 1$. In accordance with Remark 2.1 and Example 2.2, we now simulate the far field patterns of the scattered fields on an equidistant grid with 640 points on S^1. We use the same grids for the virtual origins, the same region of interest for the reconstructions, and the same parameters for the reconstruction algorithm as in Examples 5.3–5.5, except for the parameter ε in the rebinning step, which we choose as $\varepsilon = 2$ instead of 1.3. This

Downloaded 07/07/25 to 141.52.96.24 . Redistribution subject to CCBY license

© 2025 SIAM. Published by SIAM under the terms of the Creative Commons 4.0 license

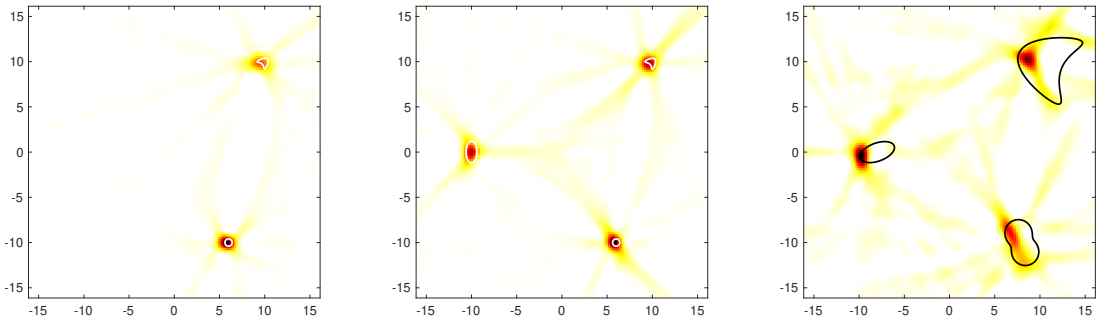

Figure 5.7. *Reconstruction from noisy data with 5% uniformly distributed relative error in Example 5.6.*

means less regularization and higher resolution. The reconstructions of the source locations obtained from noisy far field data containing 5% uniformly distributed relative additive error are shown together with visualizations of the true locations of the scatterers in Figure 5.7. The reconstructions are much clearer and sharper than in the previous examples. However, we note that the data set is ten times larger than before. The reconstructed sources are near the left boundary of the scatterers because the incident wave that we consider is a plane wave with direction of propagation $(1,0)$ propagating from left to right.

6. Conclusions. We have developed a new method to reconstruct the number and the positions of a few well-separated sources or scatterers from far field observation of a single radiated or scattered wave. The main attraction of this algorithm is that it uses only the few largest coefficients in the Fourier spectrum corresponding to the Fourier modes of low order. This part of the data set is arguably the least susceptible to measurement errors and noise.

The reconstruction method is based on rational approximation, and we utilize the poles of the corresponding rational functions to determine a sinogram of a density function which exhibits peaks near the individual supports of the sources or scatterers. These peaks are more pronounced the better the far field can be approximated by the far field radiated by a few well-separated point-sources. The well-known filtered backprojection algorithm from computerized tomography can be employed to visualize these peaks.

As has been emphasized before, the number of Fourier modes of the far field that we can use for the reconstruction is rather small, on the order of ten to twenty at most in Examples 5.3–5.5. Accordingly, the amount of work to determine the connecting lines in the plane can be considered to be about the same for every virtual origin. This means that the overall complexity of our method is linear in the number of virtual origins. Finally, the work load for the visualization of the source locations using the filtered back projection method is linear in the chosen number of pixels of the final reconstruction. Our MATLAB implementation on a standard laptop computer takes just a few seconds for any of the reconstructions shown in this paper.

While rational approximation in itself is very powerful, very little is known about the resulting poles and the information they carry. But according to our limited numerical examples, the variant of the AAA algorithm which we employ provides enough pole information to reconstruct three well-separated scatterers and seems to tolerate a decent amount of noise in

Downloaded 07/07/25 to 141.52.96.24 . Redistribution subject to CCBY license

© 2025 SIAM. Published by SIAM under the terms of the Creative Commons 4.0 license

the data. We have also observed numerically (not shown in the article) that the method can handle more than three scatterers, when they are farther than a few wavelengths apart from each other. However, the information contained in reconstructions obtained by this method, when the sources or scatterers have larger supports, is limited.

Our method requires us to choose a number of parameters, and we have provided a careful analysis to guide these choices. We warn, however, that selecting those parameters wrongly typically results in failure.

Appendix A. Here we provide an error bound for the particular approximations of the Bessel functions which form the basis of our numerical approach.

The Bessel functions $J_n(x)$ of the first kind of order $n \in \mathbb{Z}$ with argument $x > 0$ can be written as

$$J_n(x) = \sqrt{\frac{2}{\pi x}} \left(\cos\left(x - \frac{\pi}{2}n - \frac{\pi}{4}\right) P_n(x) - \sin\left(x - \frac{\pi}{2}n - \frac{\pi}{4}\right) Q_n(x) \right)$$

for some auxiliary functions P_n and Q_n (see Watson [30, sects. 7.2–7.3]). The latter possess asymptotic representations

$$P_n(x) \sim \sum_{m=0}^{\infty} \frac{(-1)^m (n, 2m)}{(2x)^{2m}} \qquad \text{and} \qquad Q_n(x) \sim \sum_{m=0}^{\infty} \frac{(-1)^m (n, 2m+1)}{(2x)^{2m+1}} \tag{A.1}$$

as $x \to \infty$, where

$$(n, \nu) := \frac{(4n^2 - 1^2)(4n^2 - 3^2) \cdots (4n^2 - (2\nu - 1)^2)}{2^{2\nu} \nu!}. \tag{A.2}$$

Truncating the asymptotic representations for P_n and Q_n from (A.1) after $p \geq 1$ and $q \in \{p-1, p\}$ terms, we can approximate P_n and Q_n by

$$P_n^{(p)}(x) := \sum_{m=0}^{p-1} \frac{(-1)^m (n, 2m)}{(2x)^{2m}} \qquad \text{and} \qquad Q_n^{(q)}(x) := \sum_{m=0}^{q-1} \frac{(-1)^m (n, 2m+1)}{(2x)^{2m+1}},$$

respectively, which gives the aforementioned approximation

$$J_n^{(p,q)}(x) := \sqrt{\frac{2}{\pi x}} \left(\cos\left(x - \frac{\pi}{2}n - \frac{\pi}{4}\right) P_n^{(p)}(x) - \sin\left(x - \frac{\pi}{2}n - \frac{\pi}{4}\right) Q_n^{(q)}(x) \right) \tag{A.3}$$

of $J_n(x)$. This approximation is well-known and recommended for large arguments (cf., e.g., [5, section 10.17]). In the following auxiliary result we provide a quantitative error estimate.

Lemma A.1. *Let $p \in \mathbb{N}$ and $q \in \{p-1, p\}$, and $N \in \mathbb{N}$ with $N > 2p$. Then, the approximation (A.3) satisfies*

$$|J_n(x) - J_n^{(p,q)}(x)| \leq \sqrt{\frac{2}{\pi x}} \frac{1}{(p+q)!} \left(\frac{N^2}{2x} \right)^{p+q} \mathrm{e}^{N^2/(2x)} \tag{A.4}$$

for every $x > 0$ and every $n \in \mathbb{Z}$ with $|n| < N$.

Downloaded 07/07/25 to 141.52.96.24 . Redistribution subject to CCBY license

© 2025 SIAM. Published by SIAM under the terms of the Creative Commons 4.0 license

Proof. Consider first the case that $0 \le n < N$. Since $p_* := \lfloor N/2 \rfloor$ and $q_* := \lceil N/2 \rceil - 1$ satisfy $2p_* \ge N-1 \ge n$ and $2q_* \ge N-2 \ge n-1$ the remainders

$$R_n(x,p_*) := |P_n(x) - P_n^{(p_*)}(x)| \qquad \text{and} \qquad S_n(x,q_*) := |Q_n(x) - Q_n^{(q_*)}(x)|$$

are no larger than the first neglected term of the respective asymptotic series (A.1) according to [30, pp. 205–206]. It thus follows that, for all p as in the lemma,

$$R_n(x,p) \le |P_n(x) - P_n^{(p_*)}(x)| + |P_n^{(p_*)}(x) - P_n^{(p)}(x)| \le \sum_{m=p}^{p_*} \frac{|(n,2m)|}{(2x)^{2m}},$$

because $2p_* \ge N-1 \ge 2p$ by our choice of N. By virtue of (A.2)

$$|(n,2m)| = \frac{|4n^2-1||4n^2-3^2|\cdots|4n^2-(4m-1)^2|}{2^{4m}(2m)!} \le \frac{1}{(2m)!}\left(\frac{4N^2}{4}\right)^{2m}$$

for every $m \le p_*$, and we therefore conclude that

$$R_n(x,p) \le \sum_{m=p}^{p_*} \frac{1}{(2m)!}\left(\frac{N^2}{2x}\right)^{2m} \le \sum_{m=p}^{\infty} \frac{1}{(2m)!}\left(\frac{N^2}{2x}\right)^{2m}. \tag{A.5}$$

As $q \le p < N/2 \le q_* + 1$ we also have $q \le q_*$, and hence we conclude similar to above that

$$\begin{aligned} S_n(x,p) &\le |Q_n(x) - Q_n^{(q_*)}(x)| + |Q_n^{(q_*)}(x) - Q_n^{(q)}(x)| \\ &\le \sum_{m=q}^{q_*} \frac{|(n,2m+1)|}{(2x)^{2m+1}} \le \sum_{m=q}^{\infty} \frac{1}{(2m+1)!}\left(\frac{N^2}{2x}\right)^{2m+1}. \end{aligned} \tag{A.6}$$

For the final inequality in (A.6) take note that $4q_* + 1 \le 4\frac{N-1}{2} + 1 \le 2N$.

Using (A.5) and (A.6), and taking into account that $q \in \{p-1, p\}$, which implies that $\min\{2p, 2q+1\} = p+q$, we see that the total error (A.4) is bounded by

$$\begin{aligned} |J_n(x) - J_n^{(p,q)}(x)| &\le \sqrt{\frac{2}{\pi x}} \sum_{m=p+q}^{\infty} \frac{1}{m!}\left(\frac{N^2}{2x}\right)^m \\ &= \sqrt{\frac{2}{\pi x}}\left(\mathrm{e}^{N^2/(2x)} - \sum_{m=0}^{p+q-1} \frac{1}{m!}\left(\frac{N^2}{2x}\right)^m\right) \\ &\le \sqrt{\frac{2}{\pi x}} \frac{1}{(p+q)!}\,\mathrm{e}^{N^2/(2x)}\left(\frac{N^2}{2x}\right)^{p+q}, \end{aligned}$$

where we have used Taylor's theorem in the final step. Thus, (A.4) holds true for $0 \le n < N$.

For negative $n \in \mathbb{Z}$ the statement now follows immediately from the fact that $J_{-n}(x) = (-1)^n J_n(x)$ and $J_{-n}^{(p,q)} = (-1)^n J_n^{(p,q)}(x)$ for every $n \in \mathbb{Z}$. ∎

Consequently, the truncated asymptotic representations $J_n^{(p,q)}(x)$ with $q \in \{p-1, p\}$ in (A.3) are good approximations of the Bessel functions for indices n which satisfy

$$|n| \le N \qquad \text{for some} \quad N \lesssim \sqrt{x}.$$

Downloaded 07/07/25 to 141.52.96.24 . Redistribution subject to CCBY license

© 2025 SIAM. Published by SIAM under the terms of the Creative Commons 4.0 license

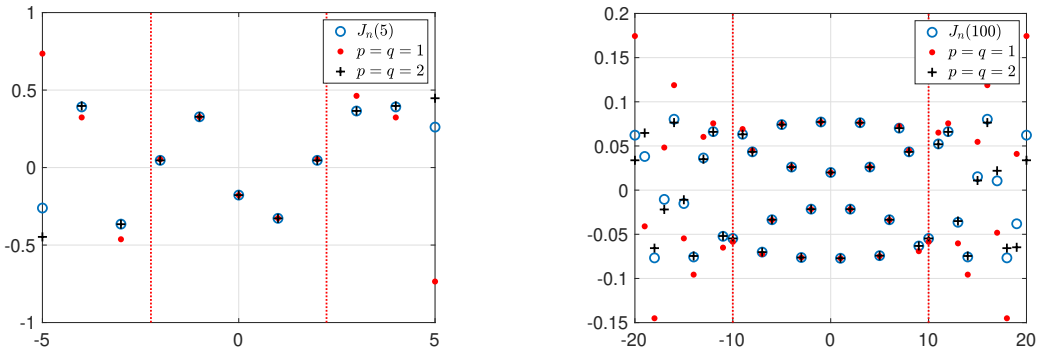

Figure A.1. *Bessel function $J_n(x)$ (blue circles) together with their approximations $J_n^{(p,q)}(x)$ as functions of n, using $p=q=1$ (red dots) and $p=q=2$ (black crosses), respectively; $x=5$ in the left hand plot and $x=100$ in the right hand plot; the dotted bars indicate the values of $\pm\sqrt{x}$.*

In this regime, even small values of p and q often yield satisfactory approximations: For instance, when $N=\lfloor\sqrt{x}\rfloor>2$ then the error bound (A.4) gives

$$|J_n(x)-J_n^{(1,1)}(x)|\le 0.21\sqrt{\frac{2}{\pi x}} \qquad \text{and} \qquad |J_n(x)-J_n^{(2,2)}(x)|\le 0.0043\sqrt{\frac{2}{\pi x}}$$

for $|n|<N$. As illustrated in Figure A.1 for two different values of x, the true errors are significantly smaller because of the alternating signs of the terms in the expansion. In fact, the values of $J_n(x)$ are well matched within the range $|n|\lesssim\sqrt{x}$, which is indicated by the dotted vertical lines in these plots.

Data availability statement. The data that support the findings of this study are openly available at the following URL/DOI: https://gitlab.kit.edu/kit/ianm/ag-ip/software/2024_Rg_Mhb_OneShotRevisited.

Acknowledgment. We acknowledge preliminary proof of concept computations by Fawad Malik during his masters thesis project. His thesis [23] is available from the authors upon request.

REFERENCES

[1] C. Alves, R. Kress, and P. Serranho, *Iterative and range test methods for an inverse source problem for acoustic waves*, Inverse Problems, 25 (2009), https://doi.org/10.1088/0266-5611/25/5/055005.

[2] N. Bleistein and J. K. Cohen, *Nonuniqueness in the inverse source problem in acoustics and electromagnetics*, J. Math. Phys., 18 (1977), pp. 194–201, https://doi.org/10.1063/1.523256.

[3] D. Colton and R. Kress, *Inverse Acoustic and Electromagnetic Scattering Theory*, 4th ed., Appl. Math. Sci. 93, Springer, Cham, 2019, https://doi.org/10.1007/978-3-030-30351-8.

[4] N. Derevianko, G. Plonka, and M. Petz, *From ESPRIT to ESPIRA: Estimation of signal parameters by iterative rational approximation*, IMA J. Numer. Anal., 43 (2023), pp. 789–827, https://doi.org/10.1093/imanum/drab108.

[5] F. W. J. Olver, A. B. Olde Daalhuis, D. W. Lozier, B. I. Schneider, R. F. Boisvert, C. W. Clark, B. R. Miller, B. V. Saunders, H. S. Cohl, and M. A. McClain, eds., *NIST Digital Library of Mathematical Functions*, Release 1.2.2, https://dlmf.nist.gov/ (15 September 2024).

Downloaded 07/07/25 to 141.52.96.24 . Redistribution subject to CCBY license

© 2025 SIAM. Published by SIAM under the terms of the Creative Commons 4.0 license

[6] A. El Badia and T. Nara, *An inverse source problem for Helmholtz's equation from the Cauchy data with a single wave number*, Inverse Problems, 27 (2011), 105001, https://doi.org/10.1088/0266-5611/27/10/105001.
[7] A. C. Fannjiang, T. Strohmer, and P. Yan, *Compressed remote sensing of sparse objects*, SIAM J. Imaging Sci., 3 (2010), pp. 595–618, https://doi.org/10.1137/090757034.
[8] L. Greengard and J.-Y. Lee, *Accelerating the nonuniform fast Fourier transform*, SIAM Rev., 46 (2004), pp. 443–454, https://doi.org/10.1137/S003614450343200X.
[9] R. Griesmaier, *Multi-frequency orthogonality sampling for inverse obstacle scattering problems*, Inverse Problems, 27 (2011), 085005, https://doi.org/10.1088/0266-5611/27/8/085005.
[10] R. Griesmaier, M. Hanke, and T. Raasch, *Inverse source problems for the Helmholtz equation and the windowed Fourier transform*, SIAM J. Sci. Comput., 34 (2012), pp. A1544–A1562, https://doi.org/10.1137/110855880.
[11] R. Griesmaier, M. Hanke, and J. Sylvester, *Far field splitting for the Helmholtz equation*, SIAM J. Numer. Anal., 52 (2014), pp. 343–362, https://doi.org/10.1137/120891381.
[12] R. Griesmaier and J. Sylvester, *Far field splitting by iteratively reweighted ℓ^1 minimization*, SIAM J. Appl. Math., 76 (2016), pp. 705–730, https://doi.org/10.1137/15M102839X.
[13] R. Griesmaier and J. Sylvester, *Uncertainty principles for inverse source problems, far field splitting, and data completion*, SIAM J. Appl. Math., 77 (2017), pp. 154–180, https://doi.org/10.1137/16M1086157.
[14] M. Hanke, *One shot inverse scattering via rational approximation*, SIAM J. Imaging Sci., 5 (2012), pp. 465–482, https://doi.org/10.1137/110823985.
[15] M. Ikehata, *Inverse scattering problems and the enclosure method*, Inverse Problems, 20 (2004), pp. 533–551, https://doi.org/10.1088/0266-5611/20/2/014.
[16] M. Ikehata, *Inverse obstacle scattering problems with a single incident wave and the logarithmic differential of the indicator function in the enclosure method*, Inverse Problems, 27 (2011), 085006, https://doi.org/10.1088/0266-5611/27/8/085006.
[17] B. Kaltenbacher and W. Rundell, *Nonlinearity parameter imaging in the frequency domain*, Inverse Probl. Imaging, 18 (2024), pp. 388–405, https://doi.org/10.3934/ipi.2023037.
[18] R. Kress, *On the numerical solution of a hypersingular integral equation in scattering theory*, J. Comput. Appl. Math., 61 (1995), pp. 345–360, https://doi.org/10.1016/0377-0427(94)00073-7.
[19] R. Kress and W. Rundell, *Reconstruction of extended sources for the Helmholtz equation*, Inverse Problems, 29 (2013), 035005, https://doi.org/10.1088/0266-5611/29/3/035005.
[20] S. Kusiak and J. Sylvester, *The scattering support*, Comm. Pure Appl. Math., 56 (2003), pp. 1525–1548, https://doi.org/10.1002/cpa.3038.
[21] S. Kusiak and J. Sylvester, *The convex scattering support in a background medium*, SIAM J. Math. Anal., 36 (2005), pp. 1142–1158, https://doi.org/10.1137/S0036141003433577.
[22] D. R. Luke and R. Potthast, *The no response test—A sampling method for inverse scattering problems*, SIAM J. Appl. Math., 63 (2003), pp. 1292–1312, https://doi.org/10.1137/S0036139902406887.
[23] F. A. Malik, *Rekonstruktion akustischer Streukörper unter Verwendung des AAA-Algorithmus*, Master's thesis, Johannes Gutenberg-Universität Mainz, 2024 (in German).
[24] Y. Nakatsukasa, O. Sète, and L. N. Trefethen, *The AAA algorithm for rational approximation*, SIAM J. Sci. Comput., 40 (2018), pp. A1494–A1522, https://doi.org/10.1137/16M1106122.
[25] F. Natterer and F. Wübbeling, *Mathematical Methods in Image Reconstruction*, Math. Model. Comput., SIAM, Philadelphia, 2001, https://doi.org/10.1137/1.9780898718324.
[26] K. Pieper, B. Q. Tang, P. Trautmann, and D. Walter, *Inverse point source location with the Helmholtz equation on a bounded domain*, Comput. Optim. Appl., 77 (2020), pp. 213–249, https://doi.org/10.1007/s10589-020-00205-y.
[27] R. Potthast, J. Sylvester, and S. Kusiak, *A range test for determining scatterers with unknown physical properties*, Inverse Problems, 19 (2003), pp. 533–547, https://doi.org/10.1088/0266-5611/19/3/304.
[28] C. Schneider and W. Werner, *Some new aspects of rational interpolation*, Math. Comp., 47 (1986), pp. 285–299, https://doi.org/10.1090/S0025-5718-1986-0842136-8.

Downloaded 07/07/25 to 141.52.96.24 . Redistribution subject to CCBY license

© 2025 SIAM. Published by SIAM under the terms of the Creative Commons 4.0 license

[29] J. Sylvester, *Notions of support for far fields*, Inverse Problems, 22 (2006), pp. 1273–1288, https://doi.org/10.1088/0266-5611/22/4/010.
[30] G. N. Watson, *A Treatise on the Theory of Bessel Functions*, Cambridge Math. Libr., Cambridge University Press, Cambridge, 1995.
[31] L. Weiss and R. N. McDonough, *Prony's method, Z-transforms, and Padé approximation*, SIAM Rev., 5 (1963), pp. 145–149, https://doi.org/10.1137/1005035.

Downloaded 07/07/25 to 141.52.96.24 . Redistribution subject to CCBY license

© 2025 SIAM. Published by SIAM under the terms of the Creative Commons 4.0 license